ORIGINAL PAPER

NaYF$_4$:Ho^{3+}/Yb^{3+}@NaGdF$_4$ core@shell upconversion nanoparticles for contrast enhancement in bimodal in-vitro OCT imaging

Kumar Shwetabh[1] · Abhishek Banerjee[2] · Raju Poddar[2] · Kaushal Kumar[1]

Abstract

Contrast enhancement is explored in optical coherence tomography images using core NaYF$_4$:Ho^{3+}/Yb^{3+} and core@shell NaYF$_4$:Ho^{3+}/Yb^{3+}@NaGdF$_4$ nanoparticles. Under 980 nm excitation, core@shell nanoparticles exhibited 2.8 and 3.3 times enhancement at 541 nm and 646 nm emission wavelengths of Ho^{3+} ions compared to core nanoparticles. Photo-thermal conversion efficiencies were 32% and 20% for core and core@shell nanoparticles. In swept-source optical coherence tomography (SSOCT), core@shell nanoparticles have shown superior contrast, while in photo-thermal optical coherence tomography (PTOCT) core nanoparticles have excelled due to their higher photo-thermal conversion efficiency. The enhancement in contrast to noise ratio obtained is 58 dB. Comparative assessments of scattering coefficients and contrast-to-noise ratios were conducted, providing insights into nanoparticle performance for contrast enhancement in optical coherence tomography.

Keywords Core-shell · Thermal decomposition · Upconversion · Photo-thermal conversion · MTT assay · OCT imaging

Introduction

Optical coherence tomography (OCT) represents a highly versatile and non-invasive cross-sectional bio-imaging modality that leverages low-coherence light interference to visualize biological samples [1]. Typically, an optical setup based on a Michelson interferometer is essential for the in vivo and in vitro examination of biological specimens. Historically, this methodology has been employed to image within turbid media, such as in retinal imaging for the early detection of ocular diseases [2, 3]. It utilizes low-coherence ultrashort light pulses, whose reflections from tissue provide valuable information regarding the time of flight or echo time delay, thereby revealing insights into the spatial distribution of tissues. A significant advancement in OCT technology comes in the form of swept-source OCT (SSOCT) and photo-thermal OCT (PTOCT), which offer notable improvements in scanning speed, sensitivity, resolution, and tissue localization compared to standard OCT [4, 5]. SSOCT, as its name implies, employs a narrow bandwidth light source with frequency-sweeping capabilities. This allows it to encode echo time delay in the light beam, subsequently detected by a low-coherence interferometer through Fourier transformation. PTOCT, on the other hand, capitalizes on the photo-thermal conversion property of tissues or contrast agents [6].

Normally SSOCT suffers low contrast in recorded images but when some specific particles are infused into the tissue the binding between the tissue surface and particles causes a refractive index mismatch between cellular boundaries which causes a phase contrast in different regions of cells [7]. Additionally, this change in refractive index creates a difference in scattering cross-section between cellular boundaries which eventually leads to enhancement in contrast. In PTOCT, the imaging is based on the heat generation from tissue upon laser irradiation. To increase the heat generation in tissue surrounding various attempts have been made. To increase contrast in OCT imaging TiO$_2$ and some metal nanoparticles can be utilized but low absorbance has limited their applicability [8, 9]. Metal nanoparticles have relatively higher photo-thermal conversion ability but haven't been able to resolve the issue

✉ Kaushal Kumar
kkumar@iitism.ac.in

1 Optical Materials and Bio-Imaging Research Laboratory, Department of Physics, Indian Institute of Technology (Indian School of Mines), Dhanbad, Jharkhand 826004, India

2 Biophotonics Lab, Department of Bioengineering and Biotechnology, Birla Institute of Technology, Mesra, Ranchi, Jharkhand 835215, India

due to the low penetration depth of excitation radiation in the visible region [10, 11]. Some efforts have been devoted to developing quantum dots as contrast enhancers but the toxicity of these materials limits their uses [12]. Similarly, organic dyes have been also tested for this purpose but low chemical and thermal stability hindered their applicability [13]. An alternative approach relies on rare earth ions doped within inorganic host lattices, which are excited by near-infrared (NIR) light. These unique molecules demonstrate exceptional resilience against photo-bleaching and photo-degradation effects, yield highly Stoke-shifted, narrow emission spectra, and this emission behavior remains consistent regardless of the size of the upconverting nanoparticles [14–20]. This feature provides the flexibility to tailor the size of upconverting molecules to meet specific research objectives. However, the efficiency of these UC nanoparticles is much less compared to the single photon down-shifting process but the application of NIR light to these upconverting molecules facilitates deep tissue imaging, minimizes light scattering, suppresses autofluorescence, and enhances image contrast for both in vivo and in vitro imaging purposes. Previous investigations into contrast agents for UC-based optical and magnetic imaging techniques have explored various options such as $NaYF_4$:Yb^{3+}/Er^{3+}@$NaGdF_4$, $NaYF_4$:Yb^{3+}/Tm^{3+}@$NaGdF_4$:Ce^{3+}/Eu^{3+}, $NaYF_4$:Yb^{3+}/Er^{3+}@$NaGdF_4$:Yb^{3+}/Nd^{3+}@$NaGdF_4$ etc [21–24]. These materials show good luminescence however, none of these materials have been tested for contrast enhancement in OCT imaging. Also, the photothermal conversion efficiency hasn't been reported for these materials which can demonstrate the capability in other modalities of imaging. Recent developments have shown considerable success in enhancing contrast in Optical Coherence Tomography (OCT) imaging using upconverting nanoparticles (UCNPs) [7, 20]. Mohan et al. employed $NaYF_4$:Ho^{3+}/Yb^{3+} particles to enhance contrast in swept source OCT (SSOCT) imaging, but their large and aggregated size limited resolution [20]. Our group intends to utilize UC nanoparticles to enhance contrast in various OCT techniques [7, 25]. Maurya et al. synthesized Er^{3+}/Yb^{3+} doped $NaGdF_4$ nanocrystals, which significantly improved contrast in SSOCT imaging [7]. These findings highlight the potential of UCNPs as contrast agents in OCT imaging.

In this study, we conducted the synthesis of core@shell nanoparticles composed of $NaYF_4$:Ho^{3+}/Yb^{3+} at the core and $NaGdF_4$ at the shell and examined their potential as contrast agents for SSOCT and PTOCT imaging. The reason behind selecting these core and shell materials is the similar crystal structure of core $NaYF_4$ and shell $NaGdF_4$ materials, which allows less or no defect creation at the core-shell interface. Also, the presence of Gd^{3+} in the shell layer makes the nanoparticle applicable in other imaging modalities like MRI for contrast enhancement. The doping of Ho^{3+}

results in a most intense emission in the green region which is comparatively superior to Er^{3+} doping where the intensity gets distributed in the green as well as the red region. This intense green emission can be utilized further in therapeutic applications like PDT to create reactive oxygen species by activating the photosensitizers. Previously our group reported the use of upconversion nanoparticles for contrast enhancement in SSOCT and PTOCT imaging which yielded significantly better outcomes [7, 25–27]. Furthermore, there are no reports demonstrating the effectiveness of core@shell upconversion nanoparticle structures as contrast enhancers in SSOCT and PTOCT imaging. In our study, we compared the contrast-enhancing capabilities of $NaYF_4$:Ho^{3+}/Yb^{3+} core nanoparticles and $NaYF_4$:Ho^{3+}/Yb^{3+}@$NaGdF_4$ core@shell nanoparticles for SSOCT and PTOCT imaging.

Experimental section

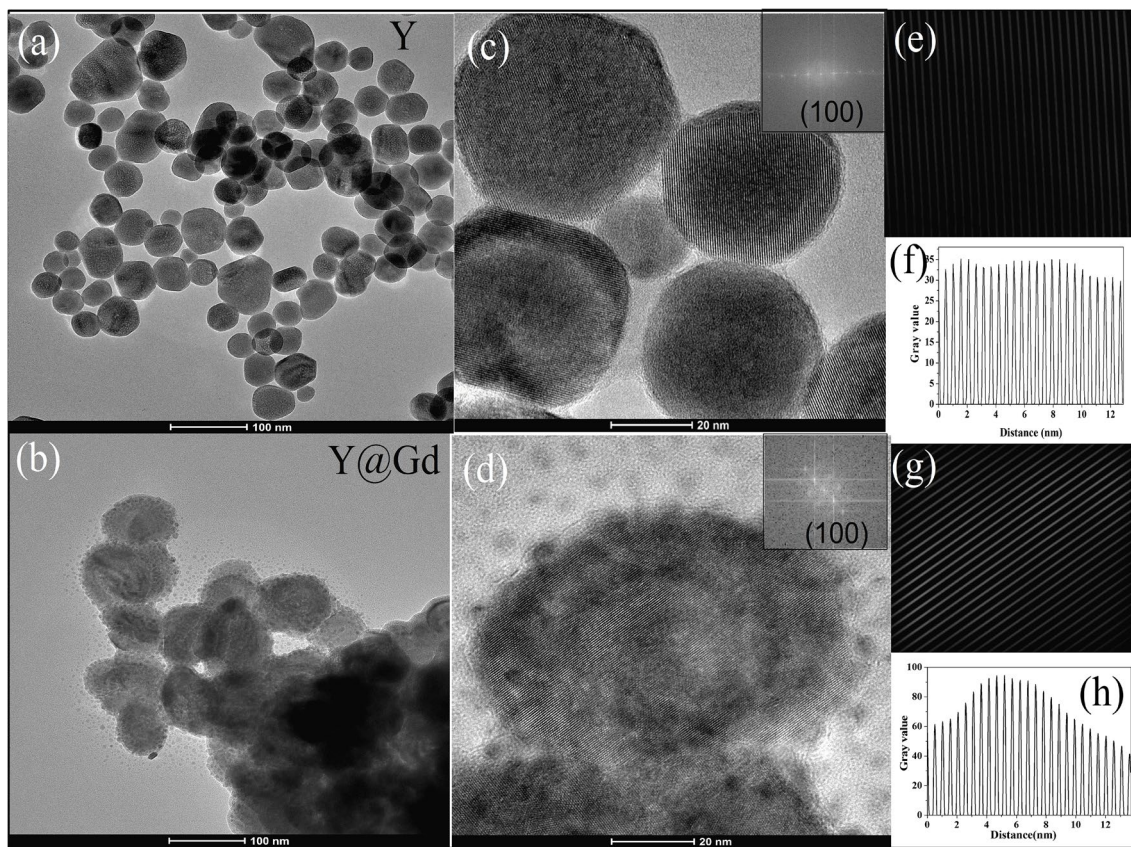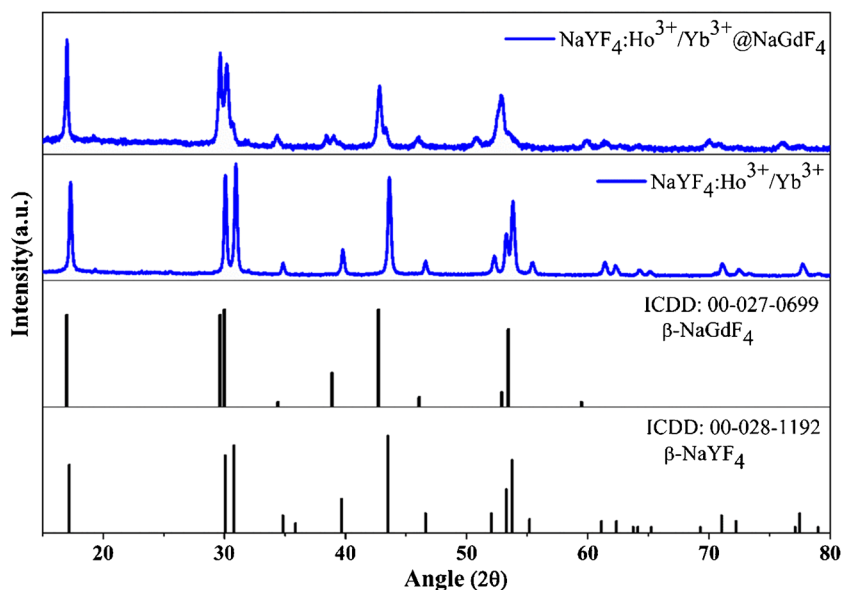The core $NaYF_4$:Ho^{3+}/Yb^{3+} and core@shell $NaYF_4$:Ho^{3+}/Yb^{3+}@$NaGdF_4$ nanoparticles are synthesized using the thermal decomposition reaction method. The concentration of Ho^{3+} and Yb^{3+} in the core was fixed at 2 mol% and 20 mol%. After synthesis, various experiments were performed to investigate the structural, morphological, and optical properties of the nanoparticles. Details of synthesis methods and other experiments performed are given in the supplementary information file.

Results and discussions

X-ray diffraction study

The powder XRD pattern of synthesized core ($NaYF_4$:Ho^{3+}/Yb^{3+}) and core@shell ($NaYF_4$:Ho^{3+}/Yb^{3+}@ $NaGdF_4$) UCNPs are shown in Fig. 1. The powder XRD pattern of core nanoparticles is matched with a hexagonal phase of $NaYF_4$ crystal whereas the diffraction peaks after shell coating are matched with the hexagonal phase of $NaGdF_4$ crystal. The core ($NaYF_4$:Ho^{3+}/Yb^{3+}) and core@shell ($NaYF_4$:Ho^{3+}/Yb^{3+}@ $NaGdF_4$) nanoparticles have a hexagonal phase pattern. There is no existence of other phases either in core or core@shell nanoparticles because all diffraction peaks correspond to the standard hexagonal pattern of $NaYF_4$ and $NaGdF_4$ crystals. The prominent peaks after shell layer coating correspond to $NaGdF_4$ crystal due to the relatively thick shell layer however there are still a few peaks of core $NaYF_4$ crystals that are visible as shoulder peaks of $NaGdF_4$ crystal in the diffraction pattern of core@shell nanoparticles. These findings confirm the formation of the desired hexagonal phase of the both core as well as inert shell layer.

Fig. 1 Powder XRD pattern of core ($NaYF_4$:Ho^{3+}/Yb^{3+}) and core@shell ($NaYF_4$:Ho^{3+}/ Yb^{3+}@ $NaGdF_4$) nanoparticles

Fig. 2 Bright-field TEM images of **a** core $NaYF_4$:Ho^{3+}/Yb^{3+}, **b** core@shell $NaYF_4$:Ho^{3+}/Yb^{3+}@ $NaGdF_4$ nanoparticles, **c** HRTEM image showing lattice fringes in core $NaYF_4$:Ho^{3+}/Yb^{3+} (inset FFT image), **d** HRTEM image showing lattice fringes in core@shell $NaYF_4$:Ho^{3+}/Yb^{3+}@ $NaGdF_4$ nanoparticles (inset FFT image), **e** inverse FFT and **f** plot profile of core $NaYF_4$:Ho^{3+}/Yb^{3+}, **g** inverse FFT and **h** plot profile of core@shell $NaYF_4$:Ho^{3+}/Yb^{3+}@ $NaGdF_4$ nanoparticles. The plot profile is used to calculate the interplanar spacing in the lattice fringe. Y and Y@Gd denote the core $NaYF_4$:Ho^{3+}/Yb^{3+} and core@shell $NaYF_4$:Ho^{3+}/Yb^{3+}@ $NaGdF_4$ nanoparticles respectively

Fig. 3 EDX map of **a** Y^{3+} and Gd^{3+} ions in HAADF mode **b** line profile of Y^{3+} and Gd^{3+} ions content which shows the presence of Y^{3+} ion in central region while Gd^{3+} ions in the outer region, **c** Y^{3+} and **d** Gd^{3+} ions in core@shell nanoparticle
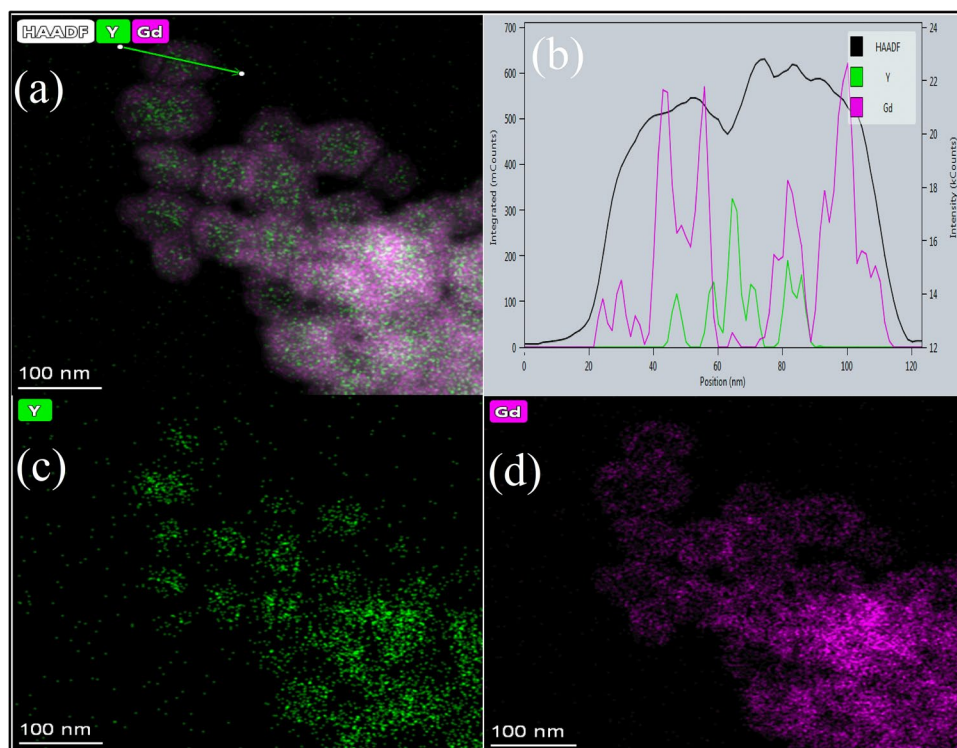

TEM imaging

The transmission electron microscopic image in Fig. 2 shows the UCNP has the morphology of nanoparticles having an average size of 47 nm for core (Fig. 2a and c) and 94 nm for core@shell (Fig. 2b and d). The shell formation leads to an increment in the size of the nanoparticles. In Bright field TEM imaging the contrast between core and shell material is very low hence it is not visualized in this imaging but we inferred the formation of core-shell structure using EDX spectroscopy in the half-angle annular dark field (HAADF)/ scanning tunneling electron microscope (STEM) imaging mode. The energy dispersive X-ray spectroscopy in the HAADF/STEM scanning mode of core@shell nanoparticles shows the presence of Y^{3+} ions only in the core while Gd^{3+} ions are present in the shell only due to the cover of un-doped $NaGdF_4$ layer. This can be regarded as proof of the formation of the core-shell structure. The enlarged image of the HRTEM of the core and shell region is given as SE1 in the supplementary information file. Figure 2e and f show the

inverse FFT pattern and plot profile of core nanoparticles while Fig. 2g and h show the inverse FFT pattern and plot profile of core-shell nanoparticles to visualize and identify the single plane across the nanoparticles.

Figure 3 shows the EDX mapping in HAADF/STEM mode that helps to visualize the formation of the core-shell structure. As we can see the Y^{3+} ion is concentrated in the core only while the Gd^{3+} ion presents only in the shell region (Fig. 3a). This is also confirmed by using a line plot across a single nanoparticle which shows the EDX peak of Y^{3+} only in the central core region while the peak corresponding to Gd^{3+} lies outside i.e. in the shell region only. From this line profile, the consistency of core and core@shell nanoparticle size can also be confirmed. The central core region has an average length of 47 nm which shows intense Y^{3+} peaks in EDX line mapping in Fig. 3b while the whole core-shell nanoparticle is around 94 nm consisting of Gd^{3+} intense peaks on the outer region. Figure 3c and d shows the EDX map of Y^{3+} and Gd^{3+} ions in core-shell nanoparticles. The EDX map of Gd^{3+} shows hollow space in the central region

Table 1 Calculated parameter values associated with the temperature profile of core and core-shell nanoparticle dispersion

Sample	Parameter	unit	Laser ON
$NaYF_4:Ho^{3+}/Yb^{3+}$	$T_{max}-T_{surr}$	°C	3.7
	τ_p	s	63.9
$NaYF_4:Ho^{3+}/Yb^{3+}@NaGdF_4$	$T_{max}-T_{surr}$	°C	5.6
	τ_p	s	136.4
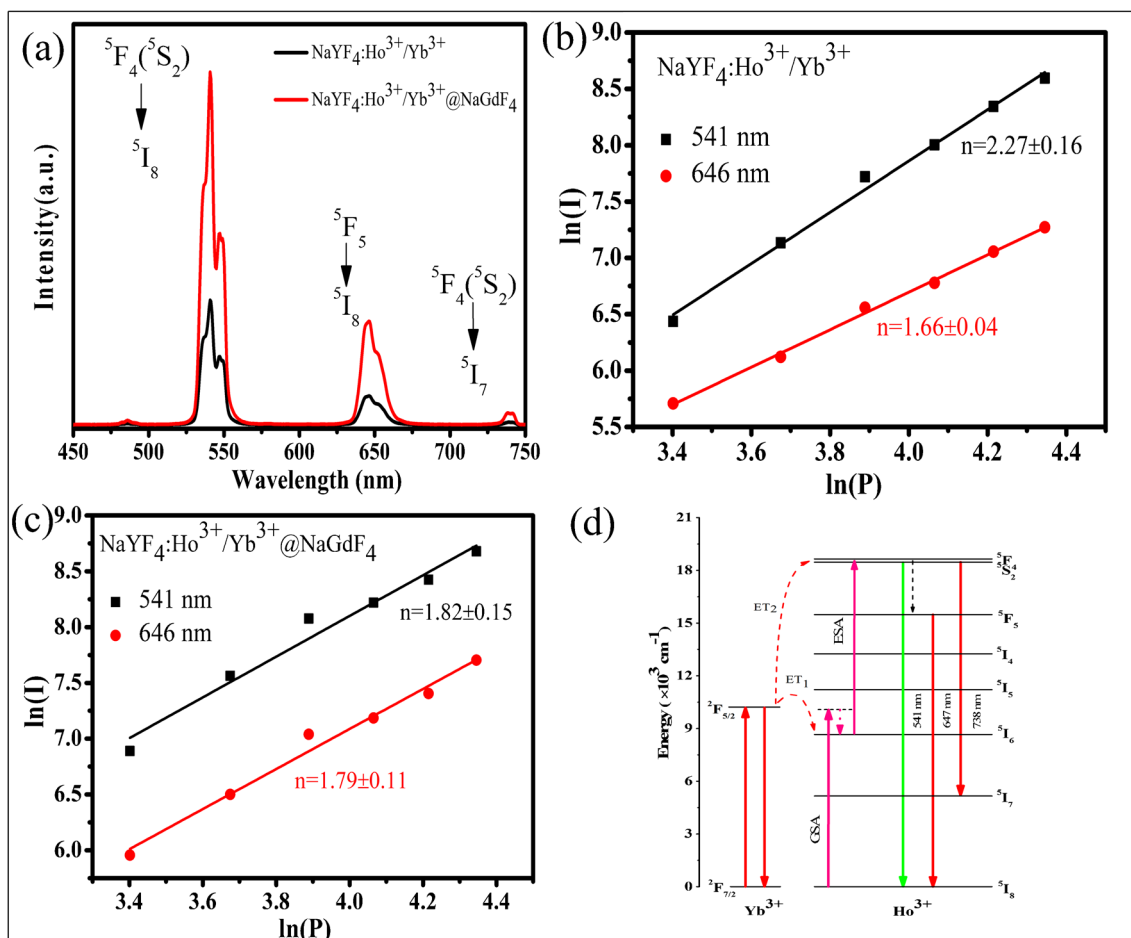
Fig. 4 **a** UC emission spectra showing enhancement in emission intensity **b**, **c** ln(P) versus ln(I) plot for calculation of number of absorbed excitation photons for core NaYF$_4$:Ho^{3+}/Yb^{3+} and core@ shell NaYF$_4$ Ho^{3+}/Yb^{3+}@NaGdF$_4$ nanoparticles respectively, **d** an energy level diagram for UC emission process in Ho^{3+}/Yb^{3+} doped system

due to the presence of Gd^{3+} ions in the shell layer. These results along with the XRD diffraction pattern discussed in "X-ray diffraction study" section confirms the formation of core@shell NaYF$_4$:Ho^{3+}/Yb^{3+}@ NaGdF$_4$ nanoparticles.

The SAED pattern for core and core-shell UCNPs was obtained which showed the distinct planes corresponding to the pure hexagonal phase of materials. The SAED pattern is given in the supplementary information file as Fig. SE2. The EDX elemental mapping was also recorded corresponding to each element and shown in the Supplementary information file as Fig. SE3.

Upconversion emission study

To study the upconversion emission property of core-shell nanoparticles, authors recorded the UC emission spectra of core and core-shell nanoparticles using 980 nm excitation wavelength. Figure 4a shows the UC emission spectra for both core and core-shell nanoparticles. The emission spectra revealed peaks at 541 nm (green) and 646 nm (red), attributed to transitions from excited energy levels $^5F_4(^5S_2)$ and $^5F_5$ to ground level $^5I_8$ within Ho^{3+} ions. A very small peak arises around 738 nm which is due to the $^5F_4(^5S_2) \rightarrow$ $^5I_7$ transition of Ho^{3+} ions. Coating the core with an inert shell enhanced the emission intensity by preventing energy migration to surface quenchers. This enhancement strategy has been previously reported [28–32]. The inert NaGdF$_4$ shell boosted green and red emissions by 2.8 and 3.3 times, respectively. Power-dependent emission spectra indicated a two-photon process for both core and core-shell nanoparticles, similar to previously reported values [33–35]. Figure 4b and c show the graph for the number of absorbed photon calculations for core and core-shell nanoparticles respectively. An energy level diagram in Fig. 4d illustrates the upconversion process, where Yb^{3+} ions initially absorbed the excitation photon, followed by energy transfer to Ho^{3+} ions. The Ho^{3+} ions then underwent transitions to emit green and red light [34, 36]. The reduction

Fig. 5 Temperature rise and decay profile for **a** NaYF$_4$:Ho^{3+}/Yb^{3+} core nanoparticles and **b** NaYF$_4$:Ho^{3+}/Yb^{3+}@NaGdF$_4$ core@shell nanoparticles in ethanol
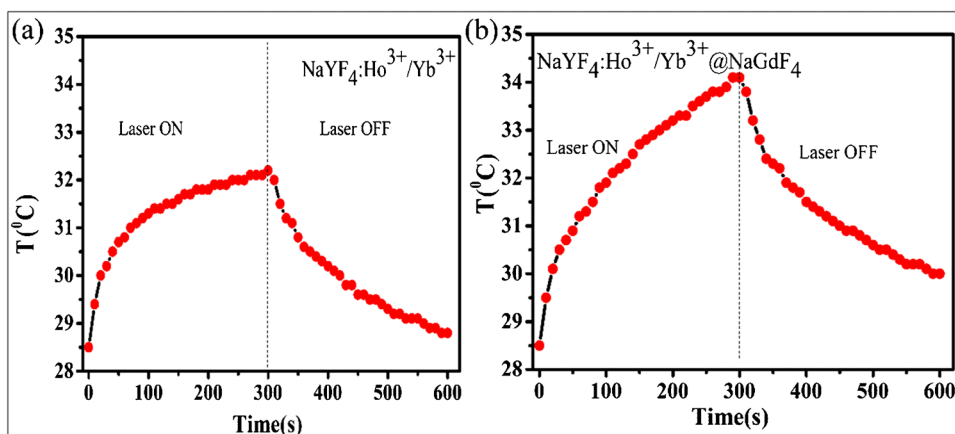
in non-radiative transitions in core-shell nanoparticles led to a decrease in photo-thermal conversion efficiency, as measured in subsequent sections.

Photo-thermal conversion study

To measure the photo-thermal conversion efficacy, both core and core-shell nanoparticles, were subjected to irradiation with a near-infrared (NIR) laser at a concentration of 4 mg/ml for 5 min, with continuous monitoring of the system temperature. Due to nonradiative transition in nanoparticle heat energy is produced. This heat conversion from the excitation of NIR photons is termed as photo-thermal conversion process. The quantification of photo-thermal conversion efficiency was executed employing Ropar's method, wherein the expression for efficiency (η) is formulated as follows [30, 31]:

$$\eta = \frac{C\frac{(T_{max}-T_{surr})}{\tau} - Q}{I(1 - 10^{-A_\lambda})} \tag{1}$$

Where C is the heat capacity of nanoparticle suspension, T_{surr} and T_{max} is the surrounding and maximum temperature respectively. Q is the heat dissipated by the cuvette medium system without nanoparticles and I is the incident excitation power. A_λ is the absorbance of nanoparticles at the excitation wavelength.

As depicted in Fig. 5, laser irradiation induces a conspicuous temperature escalation in both core and core-shell nanoparticle suspensions. Specifically, the temperature of the core nanoparticle suspension in Fig. 5a exhibits an elevation of approximately 3.7 °C after 5 min of irradiation, while the core-shell counterpart in Fig. 5b experiences an increase of about 5.6 °C. Subsequently, the photo-thermal conversion efficiency (η) of both core and core-shell nanoparticles was quantified using the Eq. (1). The nanoparticles were dispersed in ethanol and subjected

to 980 nm laser irradiation for 5 min. Subsequently, the laser was deactivated, and the dispersions underwent natural cooling to reach ambient temperature. Figure 5a and b present the acquired data, serving as the basis for calculating the conversion efficiency of core and core-shell nanoparticles, respectively. The parameters essential for the computation of photo-thermal conversion efficiency are summarized in Table 1.

Upon employing the provided parameters and Eq. (1), the calculated efficiency is 32% for NaYF$_4$:Ho^{3+}/Yb^{3+} core nanoparticles and 20% for NaYF$_4$:Ho^{3+}/Yb^{3+} @NaGdF$_4$ core@shell nanoparticles. It is noteworthy that despite the core-shell nanoparticles achieving higher temperatures, the initial temperature rise is significantly more rapid for core-only nanoparticles. This reduction in the time constant for core nanoparticles contributes to their ability to achieve a higher photo-thermal conversion efficiency, even though the overall temperature change is less than that achieved by core-shell nanoparticles. Such behavior of nanoparticles has been reported previously as well [30]. The reduction in photothermal conversion efficiency suggests that our initial assumption of reduction in non-radiative transition and hence reduction in heat generation due to an inert shell layer coating is valid. The temperature rise with and without nanoparticles in the cuvette-ethanol system is shown in Fig. SE4 of the supplementary information file.

Applications

In-vitro SSOCT and PTOCT imaging

Following the previously discussed methodology, in-vitro Swept-Source Optical Coherence Tomography (SSOCT) and Photo-thermal Optical Coherence Tomography (PTOCT) imaging were conducted. Before conducting the OCT imaging experiment, the cell viability assessment was performed using HeLa cells. Both core and core-shell nanoparticles exhibited

Fig. 6 SSOCT B-scan of (**a-d**) core and (**e-h**) core-shell nanoparticles with time. SSOCT images are recorded without using any excitation for nanoparticles
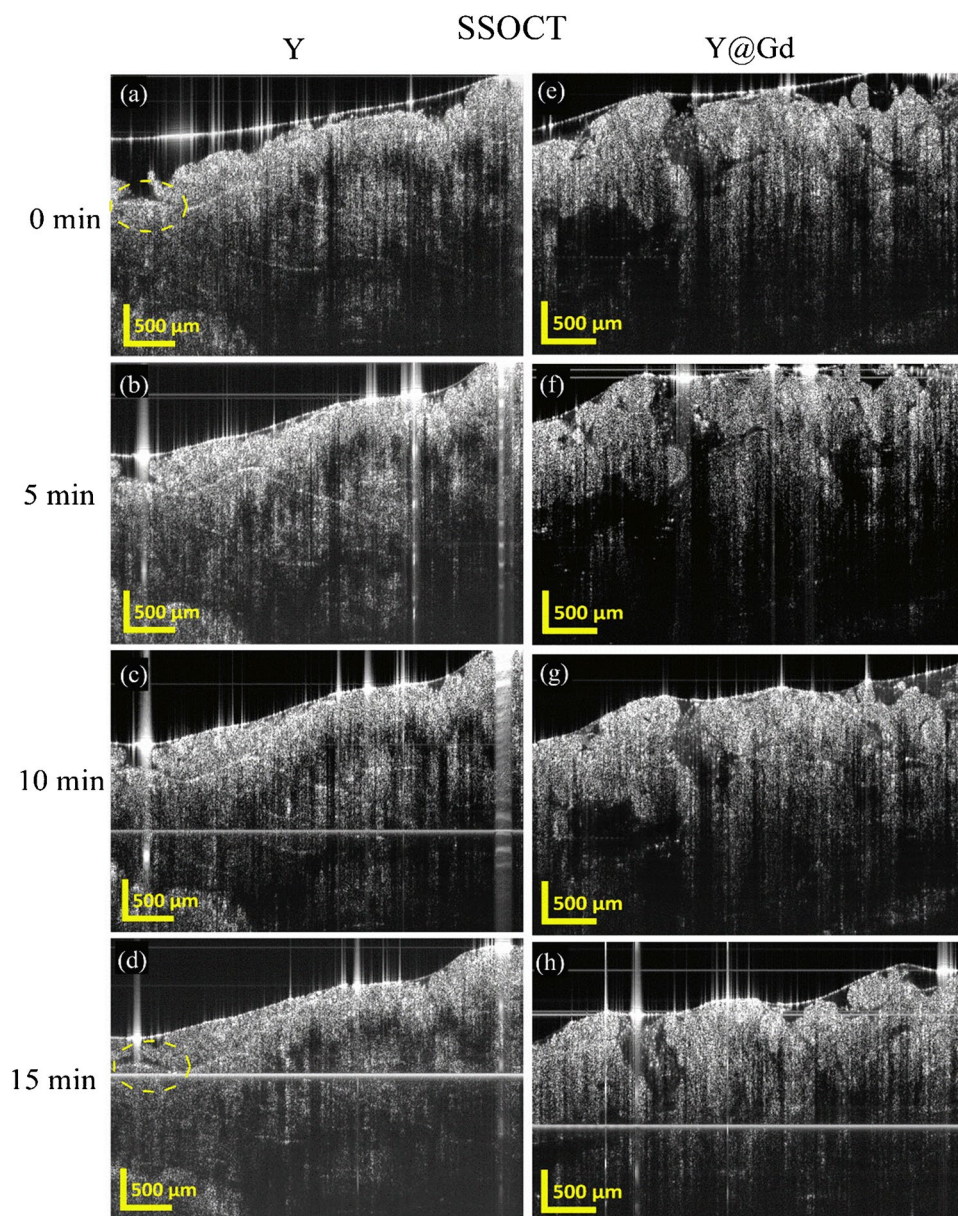
negligible toxic effects on HeLa cells, even at a substantial dosage of 250 µg/mL of UCNPs over 24 h. The results of the cell viability assessment are given in the supplementary information file as Fig. SE5. Further, a specimen of chicken breast tissue measuring 4 mm × 4 mm was employed for these imaging experiments. Subsequently, a topically applied ethanol-nanoparticles dispersion at a concentration of 50 µg/ml was introduced to the tissue. The permeation of the nanoparticles into the various layers of the chicken tissue was meticulously examined, with a focus on understanding the dynamic behavior of the nanoparticles through the scans of SSOCT and PTOCT imaging modalities. The initial column of Fig. 6 delineates the SSOCT dynamic analysis of core and core-shell nanoparticles without external excitation of nanoparticles, elucidating the inherent behavior of the nanoparticles.

Meanwhile, Fig. 7 showcases the dynamic investigation of both nanoparticle samples under excitation conditions. The progressive evolution of contrast in the SSOCT B-scan image (depicted in Fig. 6) becomes evident over time, underscoring the dynamic response of the nanoparticles within the tissue. A region in Fig. 6a and d has been circled to show the visualization of specific structures upon nanoparticle diffusion. The attachment of nanoparticles to the internal tissue structure enhances the visibility of internal structures. The application of excitation, as demonstrated in Fig. 7, not only sustains this contrast enhancement in the SSOCT B-scan image but also introduces an additional layer of contrast in the PTOCT B-scan image. This dual-modal imaging approach offers valuable insights into the spatiotemporal dynamics of the UCNPs within the intricate environment of the chicken breast tissue.

Fig. 7 PTOCT B-scan of (**a-d**) core and (**e-h**) core-shell nanoparticles with time. PTOCT images are recorded using the excitation of nanoparticles with a 980 nm laser
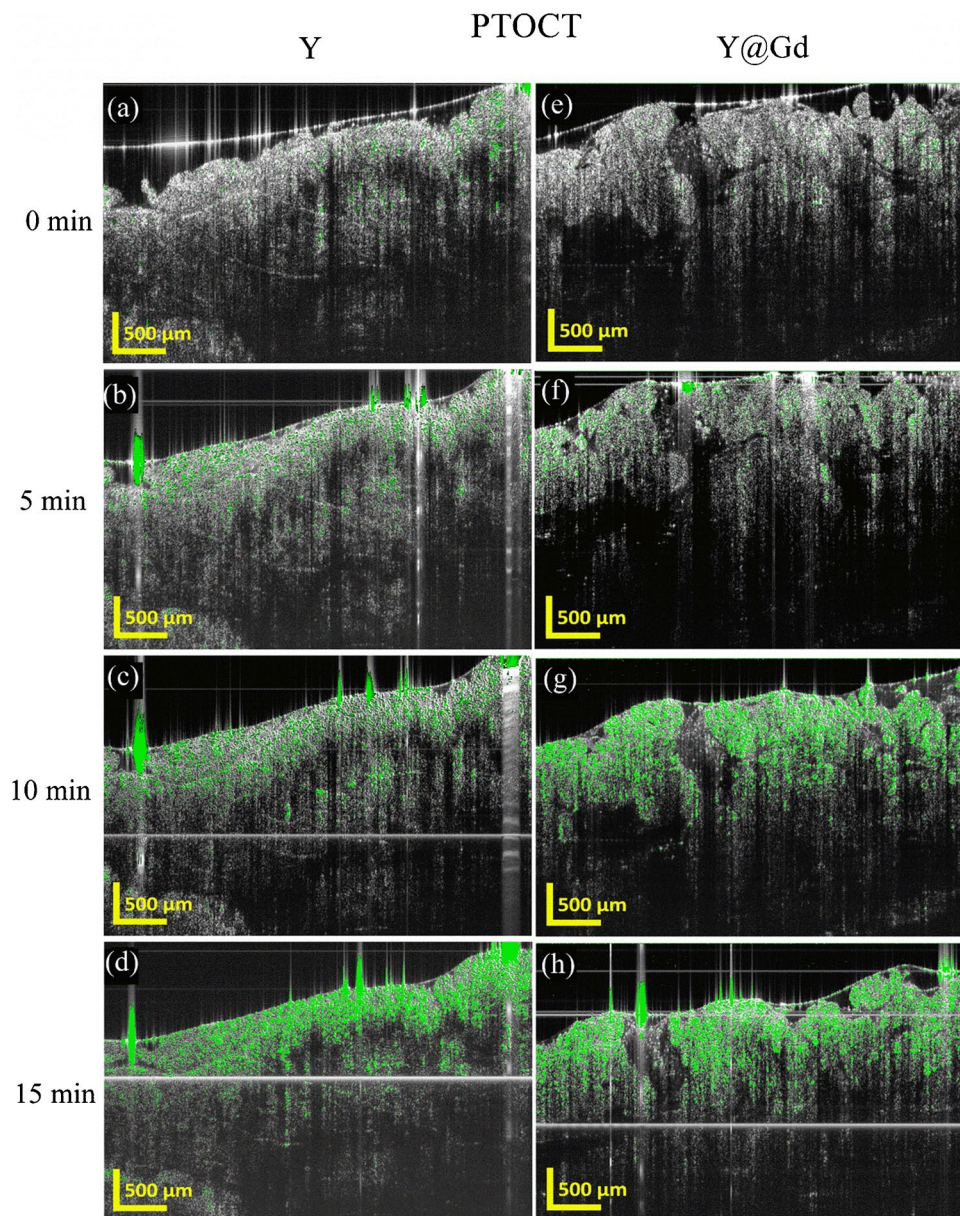

Upon a comprehensive examination of the entirety of the results presented in Figs. 6 and 7 and a discernible distinction emerges between core and core-shell nanoparticles. Notably, the core-shell nanoparticles, characterized by a diameter of approximately 94 nm, exhibit a size significantly larger than that of the core nanoparticles, which measure around 47 nm. Consequently, the increased size of the core-shell nanoparticles contributes to a heightened scattering phenomenon compared to their core-only counterparts. This nuanced difference in scattering behavior becomes particularly evident when assessing temporal evolution. Over time, the SSOCT B-scan images of the core-shell nanoparticles manifest an augmented contrast in comparison to those featuring core-only nanoparticles. The interplay of size and scattering characteristics in the core-shell nanoparticles contributes to an enhanced contrast, thereby signifying the impact of nanoparticle architecture on imaging outcomes.

In the B-scan image acquired through PTOCT, as depicted in Fig. 7, it is discerned that the photo-thermal conversion efficiency of the core nanoparticle surpasses that of the core-shell nanoparticle, as elucidated in "Photo-thermal conversion study" section. Consequently, the B-scan corresponding to the PTOCT image exhibits a heightened level of contrast for core nanoparticles compared to core-shell nanoparticles.

The preceding discourse, supported by A-scan data and rigorous mathematical analyses encompassing the determination of scattering coefficients and the computation of
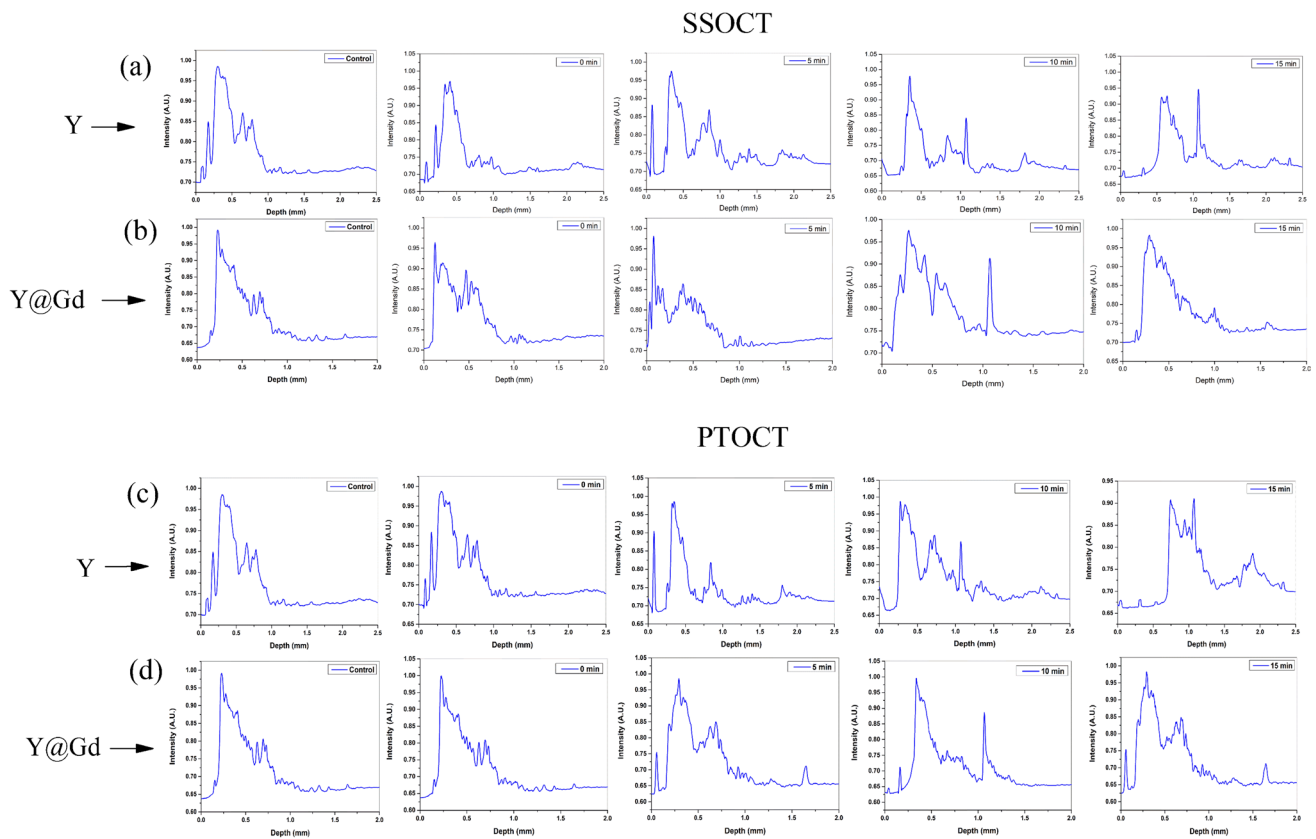
SSOCT

PTOCT

Fig. 8 **a**, **b** SSOCT A-line scan for core and core-shell nanoparticles **c**, **d** PTOCT A-line scan for core and core-shell nanoparticles

contrast-to-noise ratios (SNR), contributes substantively to our understanding. These analytical endeavors were particularly directed towards elucidating the intricate dependencies on diffusion time.

Figure 8 illustrates the A-line scan dynamics in SSOCT and PTOCT for both core and core-shell nanoparticles over time. Figure 8a and b specifically depict the A-line scan profiles in SSOCT imaging for the core and core-shell nanoparticles, respectively with time. An observation from these scans reveals a discernible trend: with the progression of time, the SSOCT signal strength experiences a more pronounced enhancement for core-shell nanoparticles compared to their core counterparts. This heightened enhancement is attributed to the larger size and improved scattering characteristics intrinsic to the core-shell nanoparticles. A comparative analysis is facilitated by referencing the A-line scan corresponding to the control sample presented in the first column of Fig. 8. Shifting the focus to the PTOCT image, as showcased in Fig. 8c and d, a differential pattern emerges. In contrast to the SSOCT findings, the signal enhancement in PTOCT is observed to occur more rapidly for core nanoparticles in

comparison to core-shell nanoparticles. This distinctive behavior is ascribed to the superior photo-thermal conversion efficiency exhibited by the core nanoparticles. The comparative analysis involves juxtaposing these outcomes with the A-line scan associated with the control sample, strategically positioned in the first column of Fig. 8.

Scattering coefficient and contrast to noise ratio estimation

Scattering, a phenomenon intrinsically tied to the material's properties, delineates the dispersion of light in alternative directions without undergoing absorption. Within this context, Beer Lambert's law asserts that the energy absorbed or transmitted through any given medium is directly proportional to the concentration of the medium, the intensity of the energy, and the path length traversed. Given that the OCT system captures echoes of 1060 nm near-infrared (NIR) light for tissue imaging, it allows for the analysis of the scattering coefficient inherent to the medium or tissue. The formulation of the OCT signal intensity is expressed as [6, 7]:

Fig. 9 Variation in CNR and Scattering coefficient value with time for **a**, **b** core nanoparticles and **c**, **d** core-shell nanoparticles respectively
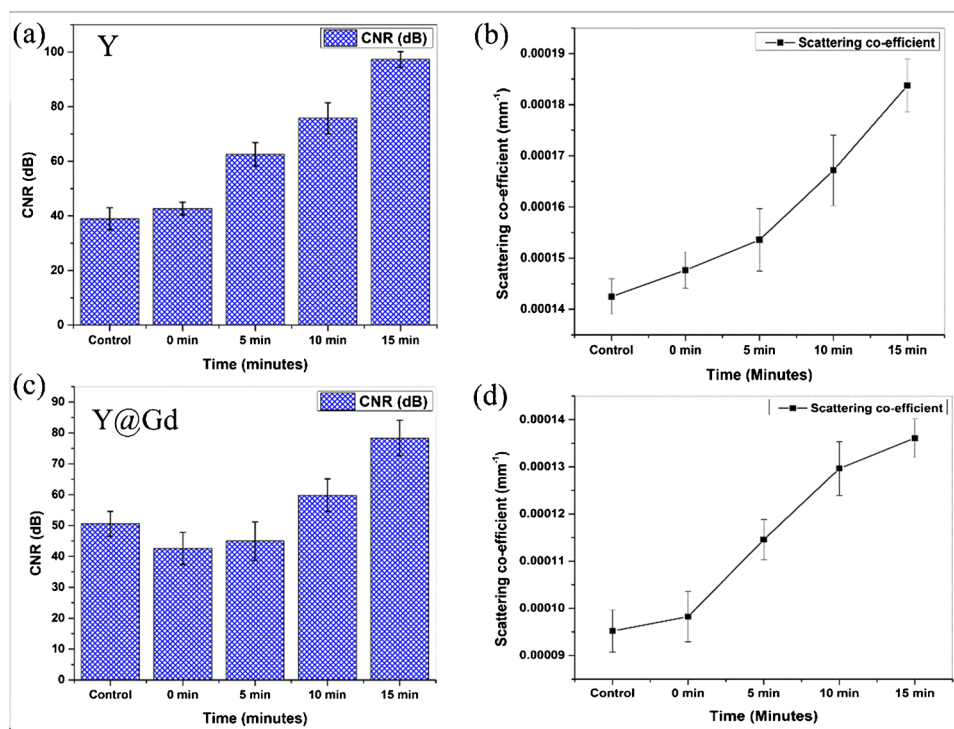
$$I(z) = I_0 e^{-2(\mu_a + \mu_s)Z} \tag{2}$$

Here, I(z) is the OCT signal as a function of depth, I_0 is zero depth intensity, z is depth, μ_s is the scattering coefficient and μ_a is the absorption coefficient, for the tissue the absorption coefficient of 1060 nm NIR light is negligible. Hence,

$$ln\frac{I}{I_0} = -2\mu_s z \tag{3}$$

The determination of the scattering coefficient involves a meticulous computational approach, wherein linear fitting of the logarithm of the A-scan intensity is executed, as extensively elucidated in our prior publication. The intricacies of this methodology are expounded upon comprehensively in our previous work. The assessment of the scattering coefficient is facilitated through the utilization of a custom-made MATLAB script, tailored to evaluate the coefficient following the given Eq. (3).

Signal to noise ratio is calculated based on the standard equation [7]:

$$CNR(dB) = 20log_{10}\left(\frac{\Delta S}{\sigma_n}\right) \tag{4}$$

Herein, ΔS represents the alteration in signal intensity observed in two distinct regions of interest (ROI) within the Optical Coherence Tomography (OCT) B-scan image, while σ_n signifies the standard deviation of the background noise. The methodology employed for ROI selection has been elucidated in our preceding research endeavors. In

summary, ROIs were systematically chosen at five distinct points of interest within the B-scan image. The standard deviation derived from these values was designated as the error bar, and the corresponding mean values were plotted accordingly. For clarity, the chosen ROIs were deliberately selected at random locations, and their standard deviations were incorporated as error bars. The mean values resulting from this selection process were then graphically represented. Figure 9 aptly illustrates the contrast-to-noise ratio (CNR) and scattering coefficient values of both core and core-shell nanoparticles. The enhancement in CNR value obtained for core nanoparticles is around 58 dB which is the highest reported according to our knowledge. Maurya et al. enhanced the CNR by 22 to 30 dB while the contrast enhancement experiment performed by Mohan et al. resulted in a CNR improvement in the range of 30–45 dB using various upconversion particles [7, 20]. These results suggest the applicability of the synthesized UCNPs as a contrast enhancer in OCT imaging. A comparison table is given in the supplementary information file as Table ST1 to compare the reported contrast enhancement using various UCNP.

Conclusions

In this study, core $NaYF_4$:Ho^{3+}/Yb^{3+} and core@shell $NaYF_4$:Ho^{3+}/Yb^{3+}@$NaGdF_4$ nanoparticles were synthesized and investigated their structural, morphological, and optical

properties. EDX mapping in HAADF-STEM confirmed the core-shell structure with a shell thickness of around 23–24 nm. Up-conversion emission spectroscopy showed significant enhancement in UC emission, especially at 541 nm and 646 nm, with enhancements of approximately 2.8 and 3.3 times, respectively, due to the NaGdF4 layer. Photo-thermal conversion efficiency was 32% and 20% for core and core-shell nanoparticles, showing the effect of the $NaGdF_4$ layer on photo-thermal conversion. Using these nanoparticles for contrast enhancement in SSOCT and PTOCT imaging revealed that core-shell nanoparticles performed better in SSOCT, while core-only nanoparticles were superior in PTOCT. The contrast enhancement using core nanoparticles was around 58dB while 30dB for core-shell nanoparticles. This study provides insights into contrast enhancement in OCT imaging using up-conversion mechanisms, suggesting the potential for developing new contrast agents.

Author contributions **Kumar Shwetabh**: Methodology, Formal analysis, Investigation, Writing-original draft, Data curation. **Abhishek Banerjee**: Formal analysis, OCT imaging. **Raju Poddar**: Analysis, Validation, Resources. **K. Kumar**: Supervision, Validation, Resources, Review & Editing.

Data availability Data will be made available on request.

Declarations

Ethical approval This research did not involve human or animal samples.

Conflict of interest The authors declare that they have no known competing financial interests or personal relationships that could have appeared to influence the work reported in this paper.

References

1. Huang D, Swanson EA, Lin CP et al (1991) Optical coherence tomography. Science 254:1178–1181. https://doi.org/10.1126/science.1957169
2. Mogensen M, Thrane L, Jørgensen TM et al (2009) OCT imaging of skin cancer and other dermatological diseases. J Biophoton 2:442–451. https://doi.org/10.1002/jbio.200910020
3. Wojtkowski M, Srinivasan V, Fujimoto JG et al (2005) Three-dimensional retinal imaging with high-speed ultrahigh-resolution optical coherence tomography. Ophthalmology 112:1734–1746. https://doi.org/10.1016/j.ophtha.2005.05.023
4. Jayaraman V, John DD, Burgner C et al (2014) Recent advances in MEMS-VCSELs for high performance structural and functional SS-OCT imaging. In: Optical Coherence Tomography and Coherence Domain Optical Methods in Biomedicine XVIII. SPIE, pp 11–21
5. Wang H, Liu W, Hu Z et al (2020) A large imaging-depth SSOCT system with one reference arm. In: AOPC 2020: Optical Sensing and Imaging Technology, vol 11567. SPIE, pp 995–999. https://doi.org/10.1117/12.2580292
6. Mohan M, Poddar R (2021) Ex-vivo molecular imaging with upconversion nanoparticles (UCNPs) using photo thermal optical coherence tomography (PTOCT). Photodiagn Photodyn Ther 33:102027. https://doi.org/10.1016/j.pdpdt.2020.102027
7. Maurya SK, Mohan M, Poddar R et al (2020) Synthesis of NaGdF4:Er3+/Yb3 + upconversion particles as exogenous contrast agent for swept-source optical coherence tomography: in vitro animal tissue imaging. J Phys Chem C 124:18366–18378. https://doi.org/10.1021/acs.jpcc.0c05786
8. Kumar A, Mondal I, Roy P, Poddar R (2018) TiO2 nanoparticles as exogenous contrast agent for 1 μm swept source optical coherence tomography: an in vitro study. Laser Phys 28:035601. https://doi.org/10.1088/1555-6611/aa9cc9
9. Mondal I, Raj S, Roy P, Poddar R (2017) Silver nanoparticles (AgNPs) as a contrast agent for imaging of animal tissue using swept-source optical coherence tomography (SSOCT). Laser Phys 28:015601. https://doi.org/10.1088/1555-6611/aa884b
10. Tucker-Schwartz JM, Beavers KR, Sit WW et al (2014) In vivo imaging of nanoparticle delivery and tumor microvasculature with multimodal optical coherence tomography. Biomed Opt Express BOE 5:1731–1743. https://doi.org/10.1364/BOE.5.001731
11. Jiang K, Smith DA, Pinchuk A (2013) Size-dependent photothermal conversion efficiencies of plasmonically heated gold nanoparticles. J Phys Chem C 117:27073–27080. https://doi.org/10.1021/jp409067h
12. Li W, Song W, Chen B, Matcher SJ (2019) Superparamagnetic graphene quantum dot as a dual-modality contrast agent for confocal fluorescence microscopy and magnetomotive optical coherence tomography. J Biophotonics 12:e201800219. https://doi.org/10.1002/jbio.201800219
13. Xu C, Ye J, Marks DL, Boppart SA (2004) Near-infrared dyes as contrast-enhancing agents for spectroscopic optical coherence tomography. Opt Lett OL 29:1647–1649. https://doi.org/10.1364/OL.29.001647
14. Chen X, Peng D, Ju Q, Wang F (2015) Photon upconversion in core-shell nanoparticles. Chem Soc Rev 44:1318–1330. https://doi.org/10.1039/c4cs00151f
15. He W, Wang M, Cheng P et al (2024) Recent advances of upconversion nanoparticles-based lateral flow assays for point-of-care testing. TRAC Trends Anal Chem 117641. https://doi.org/10.1016/j.trac.2024.117641
16. Ling H, Guan D, Wen R et al (n.d.) Effect of surface modification on the luminescence of individual upconversion nanoparticles. Small 2309035. https://doi.org/10.1002/smll.202309035
17. Chen M, Han Q, Zhang M et al (2024) Upconversion dual-photosensitizer–expressing bacteria for near-infrared monochromatically excitable synergistic phototherapy. Sci Adv 10:eadk9485. https://doi.org/10.1126/sciadv.adk9485
18. Liu S, An Z, Zhou B (2023) Optical multiplexing of upconversion in nanoparticles towards emerging applications. Chem Eng J 452:139649. https://doi.org/10.1016/j.cej.2022.139649
19. Liang W, Nie C, Du J et al (2023) Near-infrared photon upconversion and solar synthesis using lead-free nanocrystals. Nat Photon 17:346–353. https://doi.org/10.1038/s41566-023-01156-6

20. Mohan M, Poddar R (2021) Polymerically engineered upconversion nanoparticles (UCNPs) as contrast agent for functionally modified optical coherence tomography (OCT). Mater Sci Eng: C 121:111841. https://doi.org/10.1016/j.msec.2020.111841

21. Liao H, Ye S, Shi Y, Wang D (2019) Optical-magnetic bifunctional sub-20 nm β-NaYF4:Yb3+/Er3+@NaGdF4:Yb3+/Nd3+@NaGdF4 core-shell-shell nanoparticles triggered by 808 nm light. Opt Mater 98:109489. https://doi.org/10.1016/j.optmat.2019.109489

22. Meng J, Zhang Z, Zhang B et al (2019) Preparation and spectroscopic study of a water-soluble NaYF 4:yb 3+ /Er 3+ @NaGdF 4 crystal particle and its application in bioimaging. New J Chem 43:1770–1774. https://doi.org/10.1039/C8NJ05558K

23. Meng M, Zhang R, Fa X et al (2022) Core–Shell NaYF4:Yb3+/Tm3+@NaGdF4:Ce3+/Eu3+ nanoparticles for upconversion and downconversion dual-mode fluorescence-based temperature sensing. ACS Appl Nano Mater 5:9266–9276. https://doi.org/10.1021/acsanm.2c01611

24. Chen Y, Xie S, Tong C et al (2020) Preparation of NaYF4:Yb3+,Tm3+@NaGdF4:Ce3+,Eu3+ double-jacket microtubes for dual-mode fluorescent anti-counterfeiting. Trans Nonferrous Met Soc China 30:3333–3346. https://doi.org/10.1016/S1003-6326(20)65465-6

25. Shwetabh K, Maurya K, Banerjee S et al (2022) Synthesis of NaYF 4:Ho 3+ /Yb 3+ colloidal upconversion phosphor and its application for OCT-based imaging, temperature sensing, fingerprinting and security ink. New J Chem 46:21950–21961. https://doi.org/10.1039/D2NJ03878A

26. Banerjee A, Shwetabh K, Kumar K, Poddar R (2023) Exploring the effect of size variability on efficiency of upconversion nanoparticles as optical contrast agents. J Fluoresc. https://doi.org/10.1007/s10895-023-03375-0

27. Shwetabh K, Banerjee A, Poddar R, Kumar K (2024) PEG-coated NaYF4:Tm3+/Yb3+ upconversion nanoparticles for OCT image contrast enhancer, optical thermometry, and security applications. J Alloys Compd 980:173493. https://doi.org/10.1016/j.jallcom.2024.173493

28. Carl F, Birk L, Grauel B et al (2021) LiYF4:Yb/LiYF4 and LiYF4:Yb,Er/LiYF4 core/shell nanocrystals with luminescence decay times similar to YLF laser crystals and the upconversion quantum yield of the Yb,Er doped nanocrystals. Nano Res 14:797–806. https://doi.org/10.1007/s12274-020-3116-y

29. Ghosh Chaudhuri R, Paria S (2012) Core/Shell nanoparticles: classes, properties, synthesis mechanisms, characterization, and applications. Chem Rev 112:2373–2433. https://doi.org/10.1021/cr100449n

30. Xiao J-W, Fan S-X, Wang F et al (2014) Porous pd nanoparticles with high photothermal conversion efficiency for efficient ablation of cancer cells. Nanoscale 6:4345–4351. https://doi.org/10.1039/C3NR06843A

31. Mukherjee P, Tripathy S, Matsabisa MG, Sahu SK (2023) Development of upconversion-NMOFs nanocomposite conjugated with gold nanoparticles for NIR light-triggered combinational chemo-photothermal therapy. J Photochem Photobiol A 437:114426. https://doi.org/10.1016/j.jphotochem.2022.114426

32. Hao S, Yang L, Qiu H et al (2015) Heterogeneous core/shell fluoride nanocrystals with enhanced upconversion photoluminescence for in vivo bioimaging. Nanoscale 7:10775–10780. https://doi.org/10.1039/C5NR02287H

33. Joshi R, Patra S, Srivastava M et al (2022) Mesoporous NaGdF4/Ho–Yb@m-SiO2 upconversion nanophosphors as a potent theranostic probe. ACS Appl Nano Mater 5:12962–12971. https://doi.org/10.1021/acsanm.2c02782

34. Shwetabh K, Upadhyay M, Kumar M (2023) Synthesis and upconversion emission studies of CaYF 5:Ho 3+ /Yb 3+ phosphor and its applications in optical thermometry, fingerprint detection, and security ink. RSC Adv 13:9377–9386. https://doi.org/10.1039/D3RA00644A

35. Yang L, Wu H, Pan G et al (2022) Vacuum-assisted strong luminescence thermal enhancement in NaYF4:Ho3+/Yb3+ upconverting nanocrystals: a conclusive evidence for the effect of water desorption. ACS Sustain Chem Eng 10:16862–16870. https://doi.org/10.1021/acssuschemeng.2c05408

36. Chai X, Li J, Wang X et al (2017) Upconversion luminescence and temperature-sensing properties of Ho 3+ /Yb 3+ -codoped ZnWO 4 phosphors based on fluorescence intensity ratios. RSC Adv 7:40046–40052. https://doi.org/10.1039/C7RA05846B

Publisher's Note Springer Nature remains neutral with regard to jurisdictional claims in published maps and institutional affiliations.